New Journal of Physics
The open-access journal for physics

Measuring spin polarization vectors in angle-resolved photoemission spectroscopy

F Meier[1,2], **J H Dil**[1,2] **and J Osterwalder**[1,3]

[1] Physik-Institut, Universität Zürich, Winterthurerstrauss 190, CH-8057 Zürich, Switzerland
[2] Swiss Light Source, Paul Scherrer Institut, CH-5232 Villigen, Switzerland
E-mail: osterwal@physik.uzh.ch

New Journal of Physics **11** (2009) 125008 (21pp)
Received 15 May 2009
Published 11 December 2009
Online at http://www.njp.org/
doi:10.1088/1367-2630/11/12/125008

Abstract. The quantitative analysis of spin-polarized photoemission data is discussed. An angle-resolving photoelectron spectrometer equipped with a three-dimensional (3D) spin polarimeter produces complete data sets consisting of photoemission intensities as well as spin asymmetry curves for three orthogonal vector components. In a two-step fitting routine, the photoemission spectrum is first dissected into individual peaks and background. Assigning trial spin polarization vectors to each of them, the asymmetry curves can be modeled until the best fit is reached. This procedure is crucial when analyzing strongly overlapping peaks or weak signals sitting on a large unpolarized background, especially in the presence of non-collinear spins. It is robust against strong intensity variations due to matrix element effects because it references the spin polarization contribution of each band to the measured peak intensity. The method is applied to 2D systems where spin–orbit effects lead to spin splittings and complex momentum-dependent spin structures. Presented case studies include surface alloys of Bi and Pb on Ag(111) that show a giant Rashba effect.

[3] Author to whom any correspondence should be addressed.

Contents

1. Introduction

In *spintronics*, the spin of the electron rather than its charge is used to control the information flow. Spintronic components include sources of spin-polarized electron currents, gates for manipulating the spins within these currents, and electrodes that can analyze their spin polarization, as is most beautifully exemplified by the concept of the spin field-effect transistor of Datta and Das [1]. For realizing these components, one needs magnetic materials as reservoirs of macroscopically aligned spins on the one hand. Materials with strong spin–orbit interaction, on the other hand, provide a means to manipulate the spins of electronic states by addressing their spatial wave functions, without a need for magnetic fields. In two-dimensional electron gases (2DEGs), the Rashba–Bychkov effect [2] leads to a spin-dependent momentum shift of propagating free-electron-like states. Recently, surface alloys containing heavy metal atoms have been discovered that exhibit giant spin splittings which cannot be explained by this effect alone [3]. Moreover, exotic new phases for metallic surface states on certain bulk insulating materials with strong spin–orbit interaction, termed *topological insulators* [4], were predicted and found soon after [5]. These phases are related to the quantum spin Hall phase [6] and promise very low scattering rates for spin-polarized electron currents, and may thus provide a means to transport the spin information dissipationless over macroscopic distances. These exciting new developments call for fundamental studies of the electronic states involved and their momentum-resolved spin properties.

Angle-resolved photoemission spectroscopy (ARPES) has established itself as an important solid state and surface spectroscopy tool, providing direct information on electronic band dispersion and many-body effects among other things [7]. In this technique, the current of photoemitted electrons along a well-defined direction is recorded either as a function of kinetic energy or emission angle relative to the crystal directions. The resulting curves, named energy distribution curves (EDC) or momentum distribution curves (MDC), respectively, typically show peaks as schematically depicted in figure 1(a), sitting on top of a featureless background. The 'observables' of such a peak are the precise *position*, the peak *width* and the integrated *intensity*, not to mention more complex peak shapes arising from various effects. The peak position contains information on the energy dispersion and the energetics of the many-body effects, as described theoretically by the real part of the self-energy $\Re(\Sigma(\epsilon, \vec{k}))$, while the peak

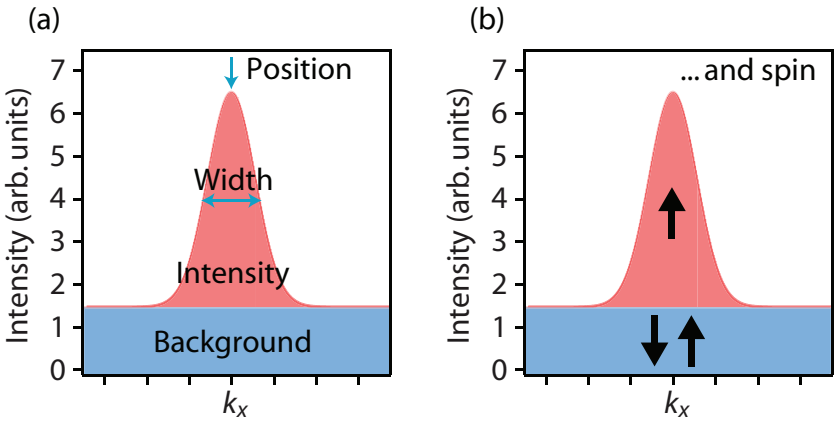

Figure 1. (a) Schematic illustration of the 'observables' in a photoemission spectrum measured at a preselected energy ϵ and momentum k_x. In (b) the spin polarization is added as an extra observable, with the typical situation of a spin-polarized peak on top of an unpolarized background.

width is a measure of the relaxation rate associated with these many-body effects, quantified by $\Im(\Sigma(\epsilon, \vec{k}))$. The intensity, on the other hand, is directly related to the photoemission matrix element, providing information on the wavefunction of the probed initial state.

The *spin* of the electron represents an extra set of observables, provided that the spin polarization of the photoelectrons can be measured as in spin-resolved ARPES (SARPES) [8]. The quantum mechanical operator governing the photoemission process does not couple directly to the electron spin, and therefore the photoelectron carries in principle, and in the absence of magnetic fields along its pathway, the spin from the initial state all the way to the detector[4]. A typical situation occurring in ARPES data from magnetic systems, or in Rashba-type systems, is depicted in figure 1(b) where a spin-polarized peak sits on top of an unpolarized background. Spin polarization is a vectorial quantity, defined as the vector of expectation values of the spin operators for a given state or ensemble of states:

$$\vec{P} = \frac{2}{\hbar}(\langle \mathrm{S}_x \rangle, \langle \mathrm{S}_y \rangle, \langle \mathrm{S}_z \rangle), \tag{1}$$

where the normalization constant $2/\hbar$ makes sure that the absolute value is $P \leqslant 1$ [9]. The spin polarization vector of a beam of photoelectrons can be described as $\vec{P} = (\mathrm{P}_x, \mathrm{P}_y, \mathrm{P}_z)$, with components

$$P_\alpha = \frac{I_\alpha^\uparrow - I_\alpha^\downarrow}{I_\alpha^\uparrow + I_\alpha^\downarrow}, \quad (\alpha = x, y, z). \tag{2}$$

Here, $I_\alpha^\uparrow$ and $I_\alpha^\downarrow$ denote the currents along the beam direction for electrons with spin parallel or antiparallel to the coordinate axis α. The spin polarization components P_α can be measured by Mott scattering off a gold target, as will be described in section 2. A complete set of SARPES data therefore consists of four quantities, the intensity $I(\epsilon, \vec{k})$ as well as $\mathrm{P}_x(\epsilon, \vec{k})$, $\mathrm{P}_y(\epsilon, \vec{k})$ and $\mathrm{P}_z(\epsilon, \vec{k})$, measured either along the energy axis (ϵ, EDC) or along some emission angle

[4] Due to spin–orbit effects in the photoemission final state, extra spin polarization can be created in the process [10]. Further sources and sinks of spin polarization in photoemission are discussed in [11].

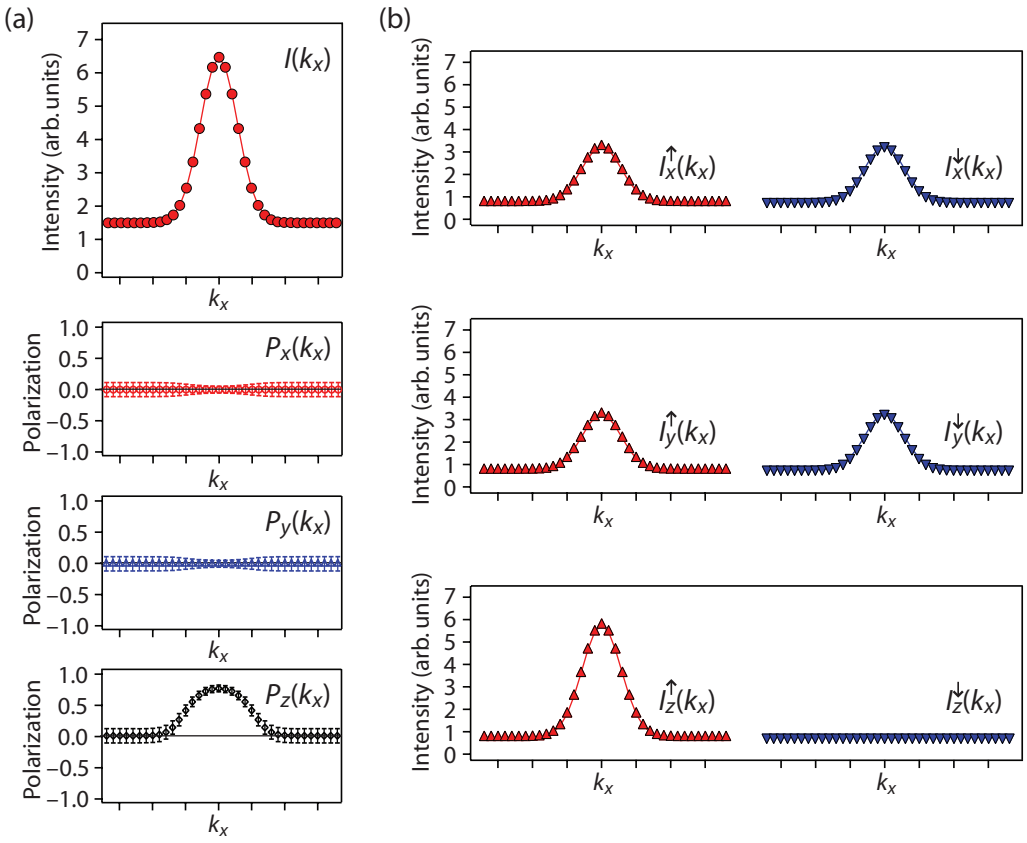

Figure 2. Illustration of the relation between the raw data measured in a SARPES experiment (a), consisting of four independent data sets, and the six spin-resolved spectra (b) that can be retrieved from them: one with spin parallel (↑) and one with spin antiparallel (↓) to the three Cartesian coordinate axes. As an example, $\vec{P} = (0, 0, 1)$ has been used for defining the spin polarization of the peak, while the background is unpolarized.

($\vec{k}$, MDC). In figure 2(a), such a complete data set has been synthesized for the case of a single peak in an MDC, resulting from a state that is fully spin polarized along the z-direction, i.e. with $\vec{P} = (0, 0, 1)$. Accordingly, the polarization spectra for the x- and y-components are uniformly zero, while the z-component shows a peak polarization that is less than one only because of the unpolarized background.

For each component, the spin-resolved spectra can be recovered from these four entities by solving equation (2) for $I_\alpha^{\uparrow}$ and $I_\alpha^{\downarrow}$, while remembering that the spin-integrated intensity is $I(\epsilon, \vec{k}) = I_\alpha^{\uparrow}(\epsilon, \vec{k}) + I_\alpha^{\downarrow}(\epsilon, \vec{k})$:

$$I_\alpha^{\uparrow}(\epsilon, \vec{k}) = I(\epsilon, \vec{k})(1 + P_\alpha(\epsilon, \vec{k}))/2 \quad \text{and} \quad I_\alpha^{\downarrow}(\epsilon, \vec{k}) = I(\epsilon, \vec{k})(1 - P_\alpha(\epsilon, \vec{k}))/2. \tag{3}$$

This is illustrated in figure 2(b) for the case at hand. From the four measured data sets, a total of six spin-resolved spectra are obtained. The physical meaning of the latter are the following: as there is no spin polarization component along the x- and y-directions, both up and down spins have equal weight in the related projections of the photoelectron current. On the other hand, the

photoelectron peak is fully polarized along the z-direction, resulting in a peak in the $I_z^{\uparrow}$ spectrum only, while the unpolarized background is equally distributed over the two projections.

The extra information contained in such spin-resolved spectra can provide very detailed information on exchange splittings and the magnetization state in magnetic systems [8], or in the case of surface states with strong spin–orbit interaction, on the splitting of Kramers pairs[5] [12], the degree of spin polarization of individual bands [13], and the detailed spin texture at the Fermi surface [14, 15]. Moreover, the spin polarization provides an extra tag in such systems that permits to observe splittings smaller than the intrinsic width of the individual peaks that could not be resolved with regular ARPES [16]. Unfortunately, this extra information does not come for free. As is briefly outlined in the next section, the measurement of spin polarization spectra is a tedious process due to the low efficiency of currently used spin detectors.

2. Experimental aspects

The ideal instrument for SARPES would involve an angle-resolving electrostatic electron energy analyzer that would select a beam of electrons with well-defined energy ϵ and momentum $\vec{k}$, feeding it into a spin separator that would count electron currents $I_\alpha^{\uparrow}$ and $I_\alpha^{\downarrow}$ separately for each coordinate axis α. Unfortunately, the concept of a simple Stern–Gerlach type spin separator does not work for charged particles like electrons [9]. The most commonly used spin polarimeters are based on the asymmetries in the Mott scattering from thin foils of a heavy metal, which is typically gold. The electron beam to be analyzed is accelerated to a few tens of kilovolts and focused onto the target foil. Two electron detectors placed symmetrically ('left' and 'right') in the backscattering direction, at scattering angles of the order of 120°, define a scattering plane. For an electron beam that is spin polarized in the direction α perpendicular to this plane, a marked asymmetry A_α is measured in the number of electrons elastically backscattered into the left (N_α^{L}) or right (N_α^{R}) detector:

$$A_\alpha = \frac{N_\alpha^{\mathrm{L}} - N_\alpha^{\mathrm{R}}}{N_\alpha^{\mathrm{L}} + N_\alpha^{\mathrm{R}}}. \tag{4}$$

The origin of this effect is the strong spin–orbit interaction that electrons experience during the backscattering process off a heavy atom [9]. For a 100% polarized beam the asymmetry is maximal and takes the value S, the so-called Sherman function[6]. The asymmetry scales linearly with the degree of polarization of the incoming beam, which can therefore be quantified as

$$P_\alpha = A_\alpha / S. \tag{5}$$

The direct measurement of the Sherman function is a tedious procedure because it requires the preparation of a beam of electrons with a well-defined degree of polarization along a specific direction [17, 18]. In section 5, a couple of calibration methods based on the analysis of SARPES data from well-characterized spin-split surface states will be discussed.

[5] A Kramers pair denotes a pair of states $\psi(\vec{k}, \uparrow)$ and $\psi(-\vec{k}, \downarrow)$ that are connected to each other by time reversal symmetry.

[6] It is termed the Sherman *function* because this value depends on the scattering energy and on the scattering angle, or the range of scattering angles, covered by the two detectors. It depends also on the quality of the Au foil. These parameters are kept fixed in a given experimental setup, and the Sherman function can thus be treated as a scalar in the data analysis.

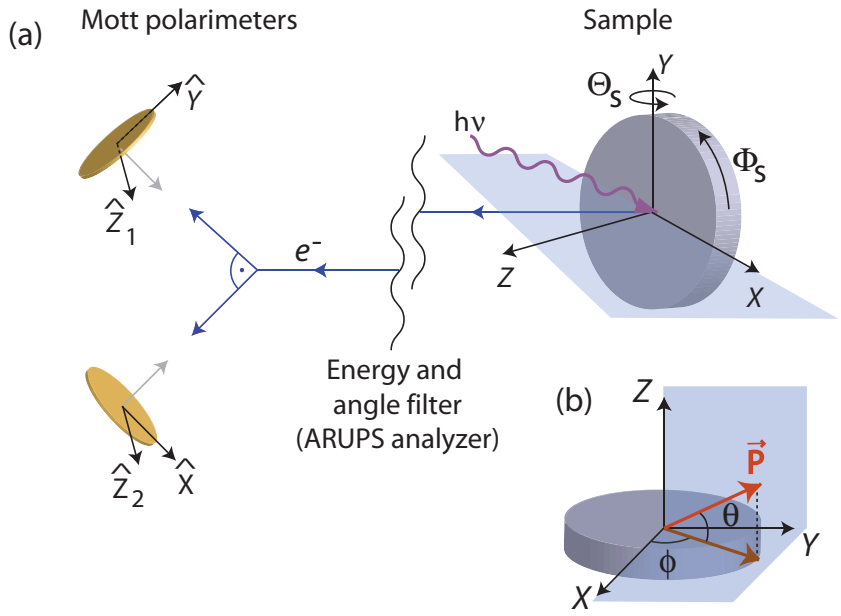

Figure 3. (a) Schematic illustration of the experimental setup for SARPES, showing on the right-hand side the sample geometry and on the left-hand side the 3D Mott polarimeter with two orthogonal gold foils. The coordinate system given by the Mott polarimeters deviates from the sample coordinates through a rotation matrix. (b) Illustration of the spin polarization vector in the sample coordinate frame.

With a second detector pair placed in a scattering plane orthogonal to the first one, the two transversal spin polarization components of the electron beam can be characterized within the same Mott polarimeter. Our group has recently built a 3D spin polarimeter based on two Mott detectors mounted in an orthogonal configuration, with an electron transfer system that takes the beam from the exit slit of an electrostatic analyzer and sends it alternatingly onto one or the other gold foil [19], as schematically shown in figure 3(a).

While these Mott polarimeters provide direct access to the spin polarization vector of an electron beam, they are very inefficient. At these high kinetic energies, the backscattering cross sections are very low, and typical effective Sherman functions S_{eff} are in the order of 6–30%.[7] Typically, to obtain the same statistical accuracy in SARPES data, acquisition times are increased by a factor of 10^3–10^4 with respect to those in regular ARPES experiments.

3. Analysis of spin-polarized ARPES data

In SARPES experiments on magnetic systems, a geometry can often be chosen such that the sample magnetization direction is aligned with the analysis direction α of one of the Mott detector pairs. The recovery of spin-resolved spectra for spin up and spin down with respect to this axis is then straightforward based on equations (3). Likewise, if the sample needs to

[7] One has to compromise between large detection solid angles, meaning higher count rates but lower S_{eff}, or small detection solid angles, with the opposite consequences [9].

be rotated on a goniometer in order to access specific locations within the band structure, the reference frame for the spin polarization of the 3D spin polarimeter can easily be rotated into the sample coordinate system (figure 3). One can then follow the sample rotation in the space of spin polarization vectors [19]. The same is true for the recording of MDCs or entire Fermi surface maps. However, in systems with strong spin–orbit interaction, it has recently become clear that situations with non-collinear spins may arise within the same spectrum, exemplified by the case of surface states on surface alloys of Bi on Ag(111), where some states are polarized mainly in the surface plane while others show considerable out-of-plane polarization [20]. The recovery of the spin polarization vector of each state then requires a vectorial approach also in the analysis of the SARPES data. A method based on the sequential fitting of intensity spectra and spin polarization spectra has recently been demonstrated by our group [13].

In this two-step fitting routine, one first analyzes the spin-integrated intensity data $I(\epsilon, \vec{k})$ by using well-established curve fitting routines with either Gaussian, Lorentzian or more complex peak shapes. Let us for the sake of clarity assume that we are dealing with MDC data scanning along k_x. The goal of this first step is to separate, for each data point, as accurately as possible the contributions from the individual bands and the background to the overall photoemission current, as is illustrated in figure 4(a). The result of the fit is then written as

$$I(k_x) = \sum_{i=1}^{n} I^i(k_x) + B(k_x), \tag{6}$$

where $I^i(k_x)$ represent the individual peaks and $B(k_x)$ the background, which in the case of MDCs can often be a constant or a simple linear function. The number of fitting parameters in this first step is then typically $3n+1$, corresponding to a value for the position, width and intensity for each of the n peaks plus a constant background.

In preparation of the second step, which is the fitting of the spin polarization spectra, a spin polarization vector $\vec{P}^i$ is assigned to each peak as

$$\vec{P}^i = (\mathrm{P}^i_x, \mathrm{P}^i_y, \mathrm{P}^i_z) = c_i(\cos\theta_i \cos\phi_i, \cos\theta_i \sin\phi_i, \sin\theta_i). \tag{7}$$

The two polar angles θ_i and ϕ_i, as well as the length of the polarization vector c_i, corresponding to the direction and the degree of polarization for each peak, will now be the fitting parameters. Their number is thus $3n$. From the total intensities and the polarization components, one can now generate the spin-resolved spectra along the three coordinate axes according to equations (3) (see also figure 2(b)). Note that for arbitrary directions of the spin polarization vector, each peak contributes to all six spin-resolved spectra as

$$I^{i,\uparrow}_x(k_x) = I^i(k_x)(1+\mathrm{P}^i_x)/2 = I^i(k_x)(1+c_i\cos\theta_i\cos\phi_i)/2, \tag{8}$$

$$I^{i,\downarrow}_x(k_x) = I^i(k_x)(1-\mathrm{P}^i_x)/2 = I^i(k_x)(1-c_i\cos\theta_i\cos\phi_i)/2, \tag{9}$$

$$I^{i,\uparrow}_y(k_x) = I^i(k_x)(1+\mathrm{P}^i_y)/2 = I^i(k_x)(1+c_i\cos\theta_i\sin\phi_i)/2, \tag{10}$$

$$I^{i,\downarrow}_y(k_x) = I^i(k_x)(1-\mathrm{P}^i_y)/2 = I^i(k_x)(1-c_i\cos\theta_i\sin\phi_i)/2, \tag{11}$$

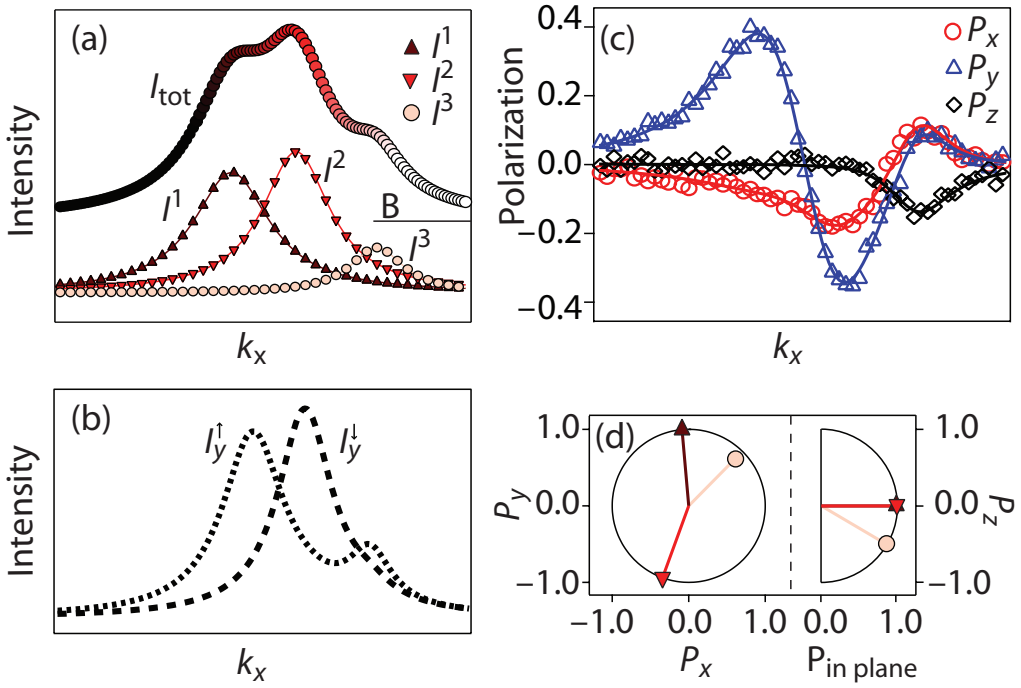

Figure 4. Illustration of the vectorial spin analysis with synthesized data. (a) Spin-integrated intensities for a MDC along k_x, showing also the peaks and the background extracted from the intensity fit. (b) Spin-resolved spectra for the y-component, which are based on arbitrarily defined spin polarization vectors for each peak. (c) Spin polarization spectra (symbols) for all three spin components, which were obtained from curves like those given in (b) by using equation (2). The lines show the spin polarization curves obtained by using the two-step fitting routine. (d) In-plane (left) and out-of-plane (right) components of the spin polarization vectors of the different peaks as obtained from the spin polarization fit. The symbols correspond to those in (a).

$$I_z^{i,\uparrow}(k_x) = I^i(k_x)(1+\mathrm{P}_z^i)/2 = I^i(k_x)(1+c_i\sin\theta_i)/2, \tag{12}$$

$$I_z^{i,\downarrow}(k_x) = I^i(k_x)(1-\mathrm{P}_z^i)/2 = I^i(k_x)(1-c_i\sin\theta_i)/2, \tag{13}$$

and the total spin-resolved spectra, e.g. along the y-direction, are thus obtained as

$$I_y^{\uparrow}(k_x) = B(k_x)/2 + \sum_{i=1}^{n} I^i(k_x)(1+c_i\cos\theta_i\sin\phi_i)/2, \tag{14}$$

$$I_y^{\downarrow}(k_x) = B(k_x)/2 + \sum_{i=1}^{n} I^i(k_x)(1-c_i\cos\theta_i\sin\phi_i)/2. \tag{15}$$

Here, the background is assumed to be unpolarized and therefore distributed evenly over the two spin-resolved spectra for each component α, as indicated in figure 2.[8] The result of this procedure is shown in figure 4(b), for polarization vectors as indicated in figure 4(d). It can be noted that peak $I^1(k_x)$ is assigned a polarization vector $P^1 \approx (0, 1, 0)$ and therefore shows up only in the $I_y^{\uparrow}(k_x)$ spectrum, while $I^2(k_x)$ points almost in the opposite direction and shows up predominantly in the $I_y^{\downarrow}(k_x)$ spectrum.

From these six spin-resolved spectra, it is straightforward to calculate point by point the spin polarization spectra along k_x by applying equation (2). The resulting curves are shown in figure 4(c), here already for the best fit to the previously synthesized spin polarization data using the same vectors $\vec{P}^i$. In the case of real SARPES data, the second step consists thus in varying these polarization vectors, defining $3n$ parameters, until the best fit to the three experimental spin polarization curves $P_\alpha(k_x)$ has been reached. Overall, this two-step routine may appear to be fitting with an enormous number of parameters. However, the two steps are carried out completely independently, with the first step corresponding to common practice in the analysis of ARPES data, and with the second step providing enormous constraints to the angles and magnitudes of the spin polarization vectors by fitting concurrently three independent SARPES curves. The benefits of this procedure will be illustrated in the following sections.

The assumption of a non-polarized structureless background may not apply to all situations, e.g. when studying magnetic systems, or when dealing with surface resonances where spin–orbit scattering in the final state might introduce spin polarization in the underlying bulk continuum. In principle, the two-step fitting routine can also deal with such situations, the pay-off being an increased number of fitting parameters required to describe the structure and polarization of the background. In the spin–orbit split surface states considered so far by our group, there was no need to include such effects in order to produce excellent fits with sensible spin polarization vectors for all bands.

The method can also be useful in a different way. There are situations where the SARPES data indicate a spin splitting of two bands by the typical up-and-down deflection of the spin polarization curve for one vector component, while the spin-integrated data do not allow to resolve two peaks. The spin can be used as a tag for identifying the individual contributions of the two split peaks. In figure 5, we analyze the sensitivity of this procedure, again by using synthesized data. The spin-integrated intensity data shown in (a) are produced by summing the two spin-resolved spectra given in the same figure, representing two fully polarized peaks of opposite spin which are separated by $\Delta k_x = 0.05\,\text{Å}^{-1}$. The result is a single peak with no indication of a splitting. On the other hand, the resulting polarization curve, calculated by using equation (2) and plotted as a red line in (b), shows a marked up-and-down deflection with an amplitude of about 0.25. The splitting of the two peaks was then varied in steps of $0.006\,\text{Å}^{-1}$ symmetrically around the initial value of Δk_x while their intensities and widths were optimized for the best fit to the original peak. All the fitted curves are contained within the marker size of

[8] This is at variance with the convention used in [13], where the scaling factors for the six spin-resolved spectra were chosen to be 1/6 such that $I(k_x) = \sum_\alpha (I_\alpha^{\uparrow}(k_x) + I_\alpha^{\downarrow}(k_x))$, i.e. the measured spin-integrated intensity $I(k_x)$ is just the sum of all spin-resolved spectra. With a scaling factor of 1/2, we have $I(k_x) = I_\alpha^{\uparrow}(k_x) + I_\alpha^{\downarrow}(k_x)$ for each spin polarization component α separately, which gives the spin-resolved spectra the meaning of a projection along a particular quantization axis α. For the shape of the spin-resolved spectra this difference is irrelevant.

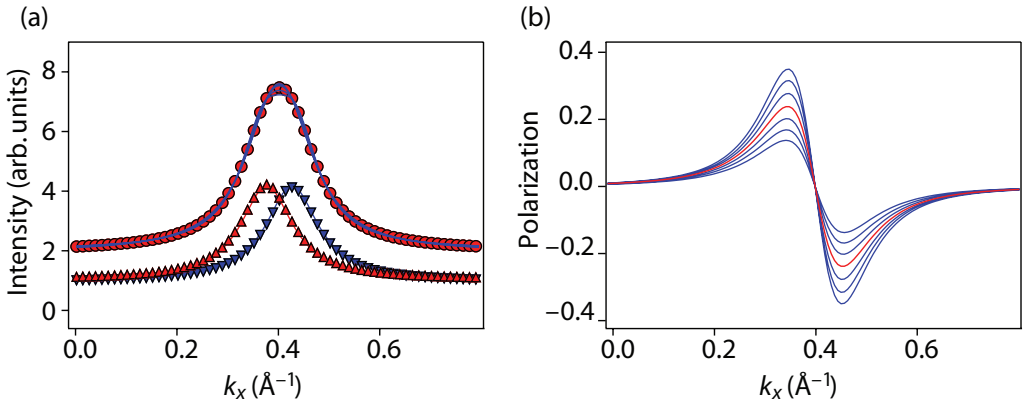

Figure 5. Synthesized SARPES MDC curves illustrating the sensitivity of such data for quantifying spin splittings. (a) Two fully and oppositely polarized peaks (up and down triangles), separated by $\Delta k = 0.05$ Å^{-1}, add up to the spin-integrated intensity data (circles). The solid (blue) lines represent best fits to the latter when the splitting is varied in steps of 0.006 Å^{-1} symmetrically around the initial value while the widths and the intensities are optimized. Except for a small region near the peak maximum, all curves fall on top of each other. (b) Variation of the spin polarization curves for the same spin splittings as in the fits in (a). The center (red) curve corresponds to the original splitting.

the latter, and it would thus be impossible to quantify the correct splitting from these data alone. However, the amplitude of the spin polarization curve is very sensitive to these small changes, with higher amplitudes for larger splittings. The effect is so pronounced because, while the peaks move apart, they also have to reduce their width in order to fit the original spin-integrated peak, thus reducing the overlap even further. For quantum well states in ultrathin Pb films on Si(111) [16], this method has been successfully applied to measure Rashba-type spin splittings in EDCs as low as 11 meV.

4. A surface alloy of Pb on Ag(111): A first example

After the first discovery of a Rashba–Bychkov effect in a metallic surface state by LaShell *et al* [21] on Au(111), showing a spin–orbit induced spin splitting larger than in the previously studied 2DEGs in semiconductor heterostructures, surface alloys of Pb and Bi on Ag(111) have more recently moved into the focus of interest [3, 22]. In these systems, a combination of several effects that go beyond the original nearly-free electron description of Rashba and Bychkov [2] lead to record high spin splittings [20, 23]. At a coverage of 1/3 monolayer, both heavy metals form $\sqrt{3} \times \sqrt{3}$-R30° surface alloy structures on Ag(111) with one Pb or Bi atom and two Ag atoms within the surface unit cell. These well-defined structures, which we henceforth refer to as Pb/Ag(111) and Bi/Ag(111), have rather similar band structures with two sets of states with negative effective masses. Both of them are spin split (figure 6(a)), leading to two sets of Kramers pairs K1 and K2. In Bi/Ag(111) the lower lying state K1 is fully occupied, thus exposing nicely the scenario of two upside-down parabolae shifted along $k_{\|}$ by the spin–orbit interaction [3]. As Pb has one electron fewer per atom, both sets of states are only partially

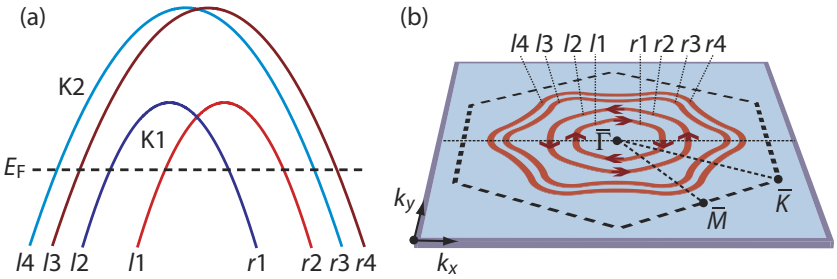

Figure 6. (a) Schematic representation of the surface state bands observed on the $\sqrt{3} \times \sqrt{3}$-R30° Pb/Ag(111) surface alloy, showing the two groups of spin-split bands associated with the Kramers pairs K1 and K2. In (b) the four Fermi surface contours related to these bands are shown inside the surface Brillouin zone, with some spin polarization vectors indicating the sense of rotation of the spins along the contours of K1.

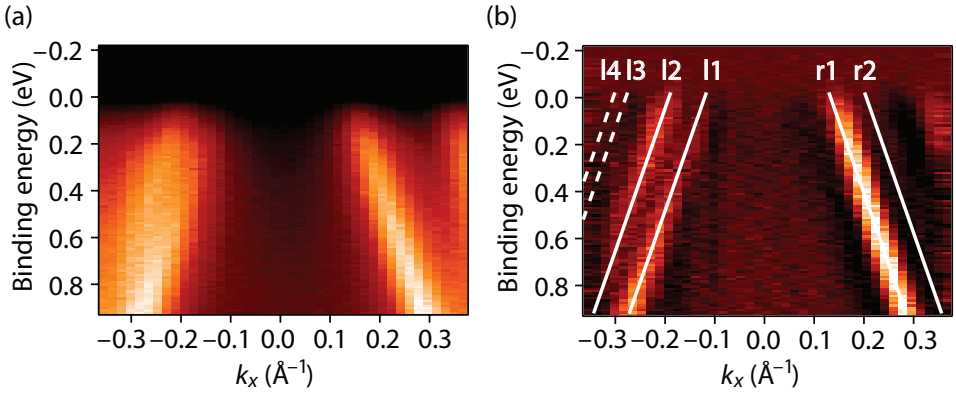

Figure 7. (a) Spin-integrated ARPES data measured with a photon energy of 24 eV, representing a cut through the surface Brillouin zone of Pb/Ag(111) along the $\bar{\Gamma}\bar{M}$-direction. (b) Second derivative of the same data. The solid lines and the corresponding labels mark the four features belonging to K1. The dashed lines mark bands belonging to K2.

occupied in Pb/Ag(111), leading to four hole-like Fermi surfaces, as schematically drawn in figure 6(b) [22].

In figure 7(a) we introduce the Pb/Ag(111) system by presenting the surface state band structure around the $\bar{\Gamma}$-point along $\bar{\Gamma}\bar{M}$, measured with spin-integrated ARPES. Figure 7(b) gives the second derivative of the same data for emphasizing the positions of the individual bands. The solid lines are shown for clarity and mark the four features '$l2$', '$l1$', '$r1$' and '$r2$' belonging to the Kramers pair K1. Due to matrix element effects, the band '$r2$' is hardly visible under these experimental conditions (see section 6). The features marked with '$l2$' and '$r1$' have spins pointing mainly along the $-y$-direction, while those of '$l1$' and '$r2$' point in the opposite direction, as already proposed by Pacilé *et al* [22]. The Rashba-type nature of this splitting was supported theoretically by Bihlmayer *et al* [23], and Meier *et al* later confirmed the spin orientations by SARPES [13].

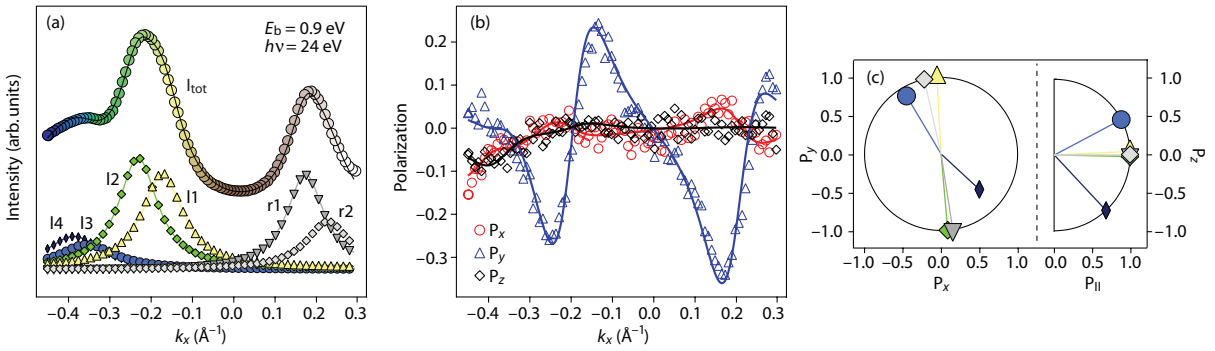

Figure 8. (a) Spin-integrated intensities of an MDC along $\bar{\Gamma}\bar{M}$ at $E_b = 0.9$ eV and the bands used for the fits. (b) Corresponding spin polarization data (symbols) and spin polarization fits (solid lines). (c) Spin polarization vectors obtained with the two-step fitting routine separated into in-plane components (left) and out-of-plane components (right). The symbols correspond to those in (a).

The second Kramers pair (K2) is barely visible in this data set. It crosses the Fermi level at higher k_x-values, marked by the dashed lines in figure 7(b). While the bands of K1 have mostly sp_z-symmetry, those of K2 are mainly p_{xy} derived. As a consequence of our experimental geometry, we only observe these bands for negative k_x, more clearly visible in the MDC given in figure 8(a). At normal emission the incidence angle of the p-polarized light on the sample is 45°. For positive k_x-values one moves towards grazing incidence and the polarization of the light moves out of the surface plane. Hence the photoelectric cross section for the p_{xy}-derived states of K2 is very low on that side.

In figure 8 we show a full set of SARPES data for Pb/Ag(111), representing an MDC along $\bar{\Gamma}\bar{M}$ at an binding energy $E_B = 0.9$ eV, and consisting of the spin-integrated intensities $I_{tot}(k_x)$ in (a) and the three polarization spectra $P_\alpha(k_x)$ given in (b). A Sherman function $S_0 = 0.085$ was used to calculate the polarization values from the measured asymmetries according to equation (5). This choice will be justified in section 5. The two-step fitting routine introduced in the previous section has been applied to these data in order to extract the spin polarization vector of each band crossed in this MDC. We used the peaks marked with $l4 - r2$, with labels in accordance with the bands shown in figure 7. The resulting spin polarization vectors are displayed in figure 8(c).

We find that the spin polarization vectors of the Kramers pair K1 lie primarily in the surface plane, with out-of-plane angles smaller than 5°. The peaks '$l2$', '$l1$', '$r1$' and '$r2$' show in-plane components that point, in that order, mainly along the $-y$, $+y$, $-y$ and $+y$-directions. Small deviations are probably due to a slight misalignment in the sample mounting, which tilts the sample coordinate frame with respect to the measurement frame. The magnitudes c_i of all four polarization vectors were fixed to one with no harm to the excellent fit to the spin polarization data (figure 8(b)). These findings are fully consistent with the scenario of the standard Rashba–Bychkov model, from which one obtains fully spin-polarized states and a tangential counterclockwise or clockwise rotation of the spins along the constant energy contours (figure 6(b)) of the outer state ('$l2$' and '$r2$') or inner state ('$l1$' and '$r1$'), respectively.

For the spin polarization vectors of the Kramers pair K2, we find significant out-of-plane spin polarizations, with rotations of up to 50° out of the surface plane and in opposite directions for '*l*4' and '*l*3', while the states remain fully spin polarized. Such finite out-of-plane spin polarization components have first been predicted by Henk *et al* [3] for similar systems. They are a consequence of the strong in-plane potential gradients in the Pb/Ag(111) system and depend on the crystallographic direction [3, 13]. This finding goes beyond the standard Rashba–Bychkov model.

5. Determination of the Sherman function

The two-step fitting routine directly accesses the spin polarization vectors associated with the individual peaks in the spectra and can thus serve as a reliable tool to determine the values intrinsic to the system at hand. However, the absolute values of spin polarization of the measured states are inversely proportional to the Sherman function S (see below), which should be known precisely. As mentioned already in section 2, the experimental determination of S is a highly complex issue [17, 18]. Here we illustrate the effect that a slight miscalibration of the Sherman function has on the spin-resolved spectra, with the previously shown SARPES data from Pb/Ag(111) as an example. Further, we suggest two simple and straightforward procedures for obtaining reliable values of S. The more precise procedure is based on the two-step fitting routine and relies, in the presented case, on the measured states to be fully spin polarized. However, it can easily be extended to systems, where the states are not fully polarized, but the degree of polarization of the states contributing to the spectrum is known. In our 3D Mott polarimeter [19], we have calibrated the Sherman function to be $S_0 = 0.085$ for each of the four detector pairs, based on measurements and two-step fitting analyses on a variety of surface states that are spin-split by the Rashba–Bychkov effect. With this value for S_0, they are all consistently found to be fully spin polarized ($c_i = 1.0$). It seems unlikely that nature has conspired to reduce the spin polarization on all these different systems by the same factor, and we therefore use this value with confidence. The relatively low value arises because the instrument uses large solid angle detectors in order to maximize the figure of merit[9] [24], and because we operate it at a comparably low 40 keV acceleration voltage for the extended measuring periods needed for SARPES.

The interdependence between the values c_i and the Sherman function can be evaluated by the relation

$$A_\alpha(k_x) = S \cdot P_\alpha(k_x) = S \cdot (I_\alpha^\uparrow(k_x) - I_\alpha^\downarrow(k_x))/I(k_x) = S \cdot \sum_{i=1}^{n} I^i(k_x) c_i \hat{P}^i_\alpha / I(k_x) \tag{16}$$

staying with the notation used in the previous sections and considering the MDC data measured along k_x. Here, we have introduced polarization unit vectors $\hat{P}^i_\alpha$. If all states i have the same degree of polarization, say $c_i =: c_0$, then the relation between the degree of polarization and the Sherman function becomes

$$A_\alpha(k_x) \cdot I(k_x) = S \cdot P_\alpha(k_x) \cdot I(k_x) = S \cdot c_0 \cdot \sum_{i=1}^{n} I^i(k_x) \hat{P}^i_\alpha. \tag{17}$$

[9] The overall efficiency of a polarimeter can be judged from the figure of merit $(I/I_0)S^2$, where I/I_0 is the ratio of detected backscattered electrons to the total number of electrons hitting the scattering target [9].

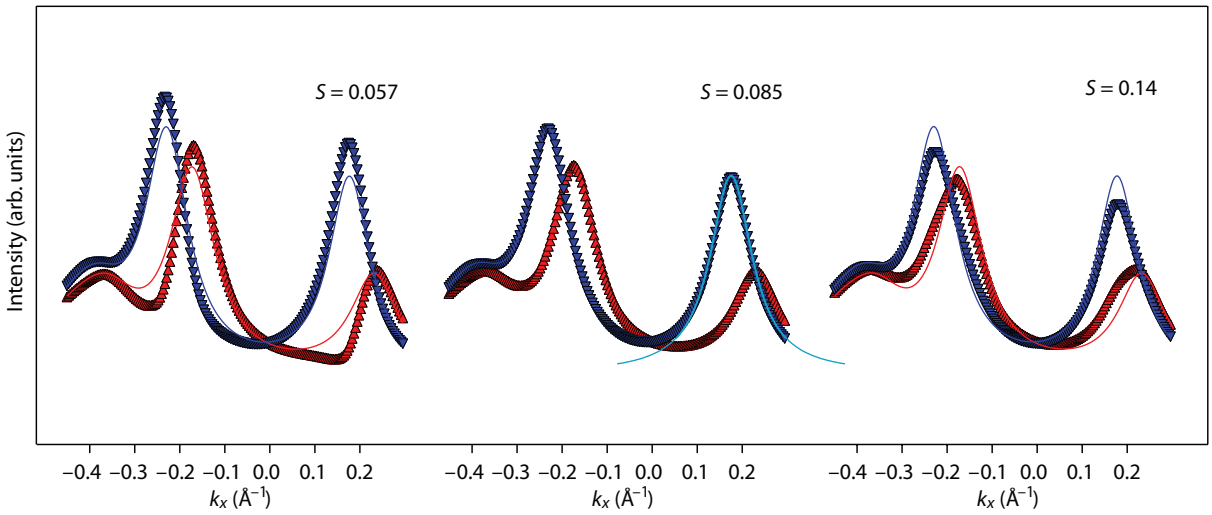

Figure 9. Intensities $I_y^{\uparrow}(k_x)$ (red) and $I_y^{\downarrow(k_x)}$ (blue) evaluated for different Sherman functions S calculated from the experimental asymmetry spectrum $A_y(k_x)$ (data of figure 8). The Sherman function of the instrument has been determined as $S_0 = 0.085$. The thin solid lines underlying the curves for $S = 0.057$ and 0.14 give the intensities for $S_0 = 0.085$ as a reference. The thin solid line under the curve for $S = 0.085$ shows one of the symmetric Voigt functions [25] used for the intensity fit.

Since both, the asymmetries $A_\alpha(k_x)$ and the spin-integrated intensities $I(k_x)$, represent measured quantities, the left-hand side of the equation remains unaffected by the analysis, and increasing the value of the Sherman function thus produces lower degrees of spin polarization c_0 in the data analysis. If the c_i values differ for different peaks in the same spectrum, the dominant peaks will see their coefficient c_i vary roughly inversely proportional to the assumed value of S.

In Rashba systems like Pb/Ag(111), the spin quantization axis obviously depends on the electron momentum. However, for the MDCs passing along the $\bar{\Gamma}\bar{M}$ line, the quantization axis has been found to be the same for the different states of the K1 manifold. This allows for a meaningful representation of the data in terms of spin-resolved intensity spectra $I^{\uparrow}(k_x)$ and $I^{\downarrow}(k_x)$ with respect to the quantization axis, which was found to be the y-axis[10]. In figure 9, we show the spin-resolved intensities calculated from real SARPES data using equations (3) and (5), and assuming different Sherman functions. Of course, this kind of representation is no longer justified for the states belonging to the Kramers pair K2, which has strong out-of-plane components, and we will thus only discuss features related to K1. In the center of the figure, the curves obtained for $S = S_0 = 0.085$ are shown. A momentum shift of 0.05 Å^{-1} between the two spin components is observed within the K1 manifold. The four peaks exhibit highly symmetric line shapes that can be well fitted with Voigt functions, as is indicated for the peak '$r1$'. When the same data is analyzed with a reduced Sherman function of $S = 0.057$, the peaks become

[10] The spin-resolved intensities in general lose their physical meaning once they refer to an axis off the quantization axis.

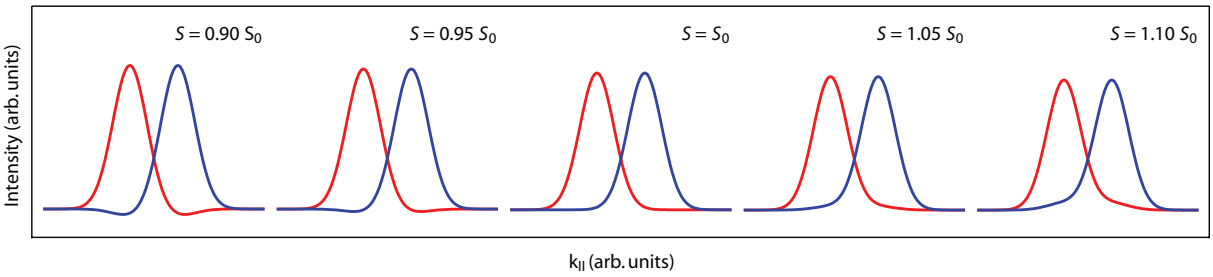

Figure 10. Spin-resolved intensities $I^{\uparrow}(k_x)$ and $I^{\downarrow}(k_x)$ calculated from the same synthesized intensity and asymmetry spectra but using different Sherman functions S as indicated. The original spectra represent two completely and oppositely spin-polarized peaks on a constant, unpolarized background, assuming a Sherman function $S_0 = 0.085$ for generating the asymmetry spectrum.

asymmetric, with steeper slopes in the regions of peak overlap, and the spin splitting is slightly increased. Intensities in one spin channel can be pulled down considerably with respect to the S_0 reference curve in regions where the other spin channel has high intensities. The opposite scenario is found when $S = 0.14$ is used in the data analysis. The spin-resolved peaks have additional intensities in regions of overlap and become strongly asymmetric. With respect to $S_0 = 0.085$, the spin splitting is slightly reduced in this case.

These effects can be brought out more clearly in synthesized spectra, modeling a simpler situation with only two peaks of opposite spin polarization sitting on a constant background (figure 10). A lowering of the Sherman function leads to unphysical negative intensities in the regions of peak overlap, while too high a value produces asymmetric peak broadening. The figure indicates the kind of statistical accuracy that one needs in order to determine the true Sherman function with a precision of 5%. Considering the values of S given in figure 9, this procedure is in general not very precise for real data. Nevertheless, this analysis indicates that the spin-resolved spectra, and in particular the spin splittings, are relatively robust with respect to quite large variations in the Sherman function.

The method described so far is entirely model independent, but is limited by the modest statistical accuracy that is usually obtained in SARPES data due to the poor detector efficiencies. The situation can be improved by using the two step fitting routine, because the statistical error in the fitted spin polarization vectors, and hence in the spin-resolved spectra, is significantly smaller than the statistical error in the raw SARPES data because the two-step fitting routine addresses an ensemble of data points. Moreover, the fit parameters c_i represent an independent check for the correctness of the Sherman function: according to equation (17) the values of c_i vary inversely proportional to the value of S. Since the degree of spin polarization cannot exceed 100% ($c_i = 1.0$), the fitting can provide an absolute lower limit for the Sherman function. In other words, the asymmetry amplitude measured in the raw data requires a minimum Sherman function for it to be physical. If we believe in theoretical predictions that spin-split bands in clean 2D Rashba systems, like the surface state on Au(111) or the K1 manifold in Pb/Ag(111), are 100% spin polarized [23, 26], or if we know the degree of spin polarization c_i of certain bands, we obtain a direct measure for the Sherman function. This is how we determined our value of $S_0 = 0.085 \pm 0.003$. Of course, the reliability of this procedure depends crucially on

the quality of the curve fitting in the first step. A similar method was applied recently for the absolute calibration of a spin polarimeter behind a time-of-flight spectrometer for laser-excited SARPES, using Au(111) as a reference sample [27].

6. Extraction of spin polarization vectors in the presence of strong matrix element effects: Bi/Ag(111)

The measured intensity of a peak depends strongly on several parameters such as measurement geometry, symmetry of the initial state wavefunction, photon beam polarization and excitation energy. These effects are described by the matrix element in correspondence to the transition matrix in Fermi's golden rule [7]. A major advantage of the two-step fitting routine is that it references the spin polarization of a particular peak to its intensity. By this means we can extract meaningful spin polarization vectors of individual states, independent of the peak-to-background ratio or possible overlap with adjacent states. The method is thus robust against strong intensity variations due to matrix element effects, as will be illustrated in this section.

In figure 11(a), we present schematically the surface state band structure of Bi/Ag(111), which is closely related to that of Pb/Ag(111) (see section 4). Here, the Kramers pair K1 is fully occupied due to the extra electron in Bi with respect to Pb, and the spin splitting is even larger than in the former case. The predominant band symmetries are also similar, namely sp_z-like for K1 and p_{xy}-like for K2.

Spin-integrated ARPES data from the Bi/Ag(111) surface alloy are shown in figures 11(b)–(g), measured at different photon energies. Surface states show no dispersion as a function of the $\vec{k}$ -vector component normal to the surface, here k_z. Therefore, the dispersions $\epsilon(k_x)$ of the Kramers pairs K1 and K2 remain unaffected by changing the photon energy. However, dramatic changes are observed in the relative intensities of the subbands, marking very strong matrix element effects in this system. For instance, changing the photon energy by only 2 eV from 23 to 25 eV shifts most of the spectral weight from the state '$r1$' to the state '$l1$' (associated with K1), even close to the $\bar{\Gamma}$ point. Because the two states have similar wavefunctions but opposite spin polarization [13], we conjecture that spin selection rules rather than band symmetries dominate the transition probabilities. These strong spin-dependent transition matrix elements near normal emission suggest the presence of spin-polarized final states, most likely as a consequence of strong spin–orbit coupling [26].

In these data sets it is difficult to distinguish the states '$l3$' and '$r3$' of K2 from the outer states '$l2$' and '$r2$' of K1. For a more quantitative comparison we show in figure 12 the intensity variations described above for different MDCs at a binding energy of 0.9 eV. From these MDCs it becomes more obvious that there are also intensity variations of K2 states, and that at a photon energy of 21.2 eV one sees mainly the '$l3$' state on the left-hand side, while at 24 eV it is the '$l2$' state. In the following, we will use these MDCs in order to illustrate the effect that these pronounced intensity changes have on the spin polarization spectra.

In figure 13, we show SARPES MDC data from Bi/Ag(111) along the $\bar{\Gamma}\bar{M}$ line at a binding energy $E_b = 0.9$ eV, measured with a photon energy of 24 eV. The spin-integrated intensities are shown in figure 13(a), together with the bands used for the two-step fitting routine. The spin polarization vectors obtained by fitting the spin polarization data of figure 13(b) are given in figure 13(c). They show strong similarities to those found on the Pb/Ag(111) surface alloy for corresponding states. Specifically, the states belonging to K1 are mostly polarized in the surface

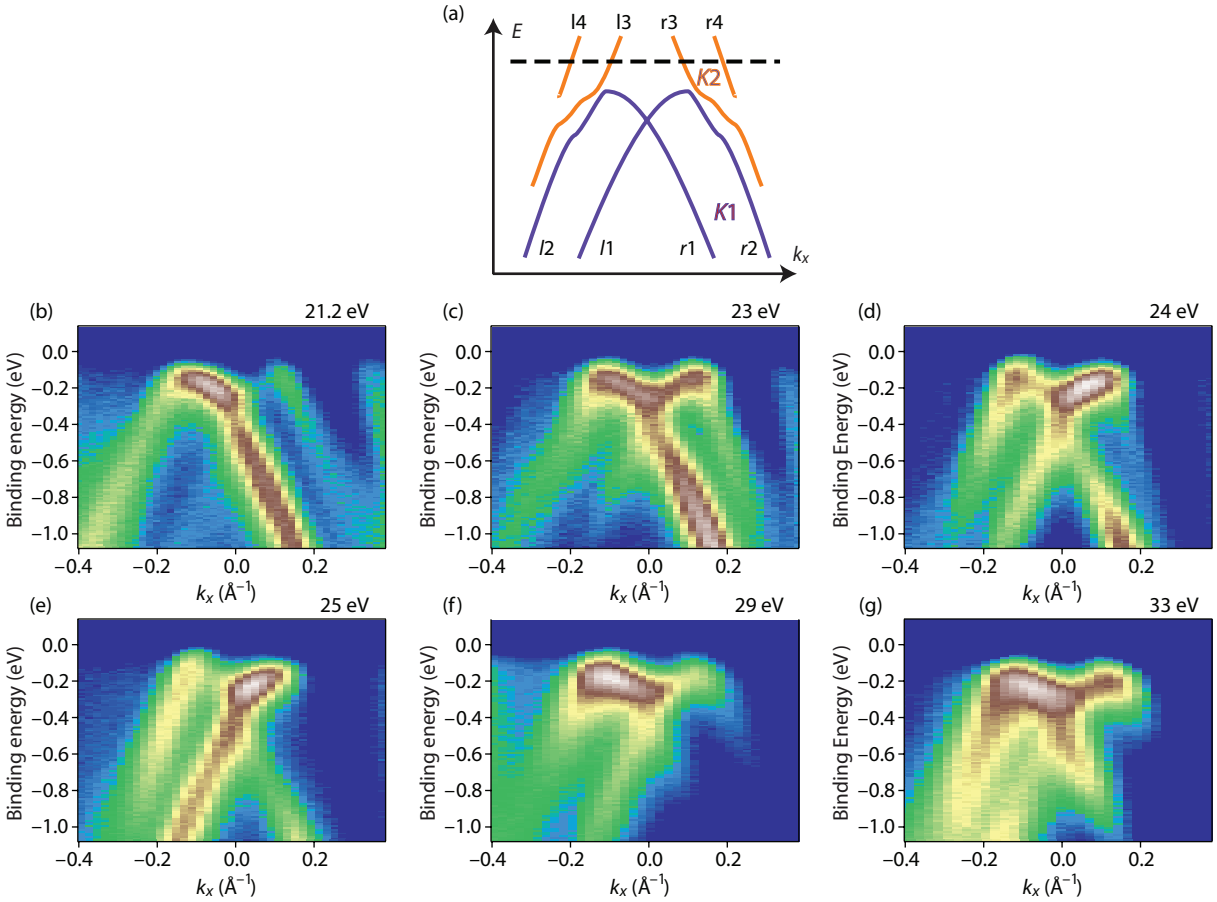

Figure 11. (a) Schematic surface state band structure of Bi/Ag(111) (adapted from [23]), showing the two Kramers pairs K1 and K2 and the band labeling convention. (b)–(g) Spin-integrated ARPES data representing cuts through the surface Brillouin zone of Bi/Ag(111) along the $\bar{\Gamma}\bar{M}$-direction, measured at different photon energies as indicated above each panel.

plane, with spin polarization vectors rather well aligned with the y-axis. The peak '$l3$', which is p_{xy} derived, shows a strong out-of-plane component in this direction of the surface Brillouin zone. The rotation out of the surface plane is larger than for Pb/Ag(111), we find out-of-plane angles of up to 70°.

The analysis of the data shown in figure 13 provided us with the spin polarization vectors of the five bands crossed in this particular MDC. These vectorial quantities are properties of the surface alloy system under investigation and should therefore not depend on the photon energy at which they are measured[11]. We can thus use these vectors in order to predict what the SARPES data corresponding to the MDCs of figure 12 should look like. The spin polarization curves for the different photon energies are calculated in two steps. First, the spin integrated intensities of figure 12 were fitted with five peaks corresponding to states '$l3$'–'$r2$'. Subsequently the spin polarization vectors found from the data set measured at 24 eV were assigned to the

[11] We assume here that there is no change of spin polarization occurring due to the photoemission process, an assumption that holds only approximately. Theory predicts some effects of this kind [26].

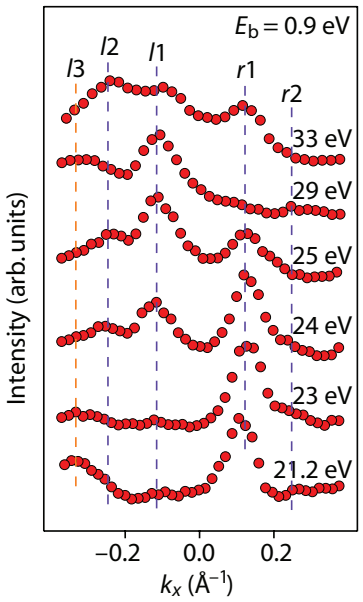

Figure 12. Spin-integrated MDCs at $E_b = 0.9$ eV for different photon energies, extracted from the data of figure 11. The dotted lines indicate the positions of the different bands.

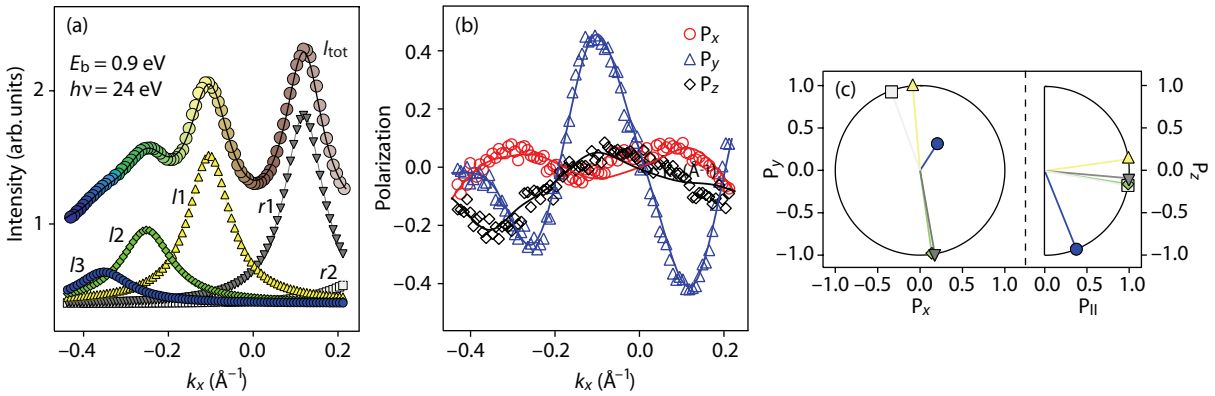

Figure 13. (a) Spin-integrated intensities of an MDC along $\bar{\Gamma}\bar{M}$ at $E_b = 0.9$ eV and the bands used for the fits. (b) Corresponding spin polarization data (symbols) and spin polarization fits (solid lines). (c) Spin polarization vectors obtained with the two-step fitting routine separated into in-plane components (left) and out-of-plane components (right). The symbols correspond to those in (a).

corresponding states, and the six spin-resolved spectra were calculated using equations (8)–(13). The spin polarization curves for the three coordinate axes then result directly from equation (2).

Figure 14 displays the curves obtained for five different photon energies. They look dramatically different. At 21.2 and 23 eV, where the state '$r1$' dominates the intensity spectrum, the negative spin polarization along the y-direction dominates the polarization spectrum. At

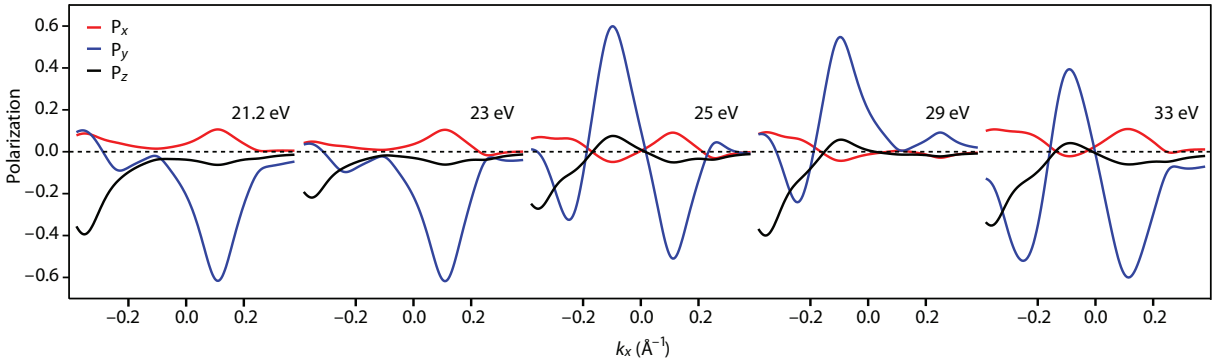

Figure 14. Spin polarization curves synthesized for different photon energies corresponding to the MDCs shown in figure 12, and using the spin polarization vectors found from the measurements at a photon energy of 24 eV (figure 13).

29 eV the situation is reversed and the state '$l1$' dominates with a positive y polarization. The K2 derived '$l3$' state contributes strongly to the z polarization spectrum. From this analysis it becomes evident that a well chosen photon energy, and binding energy for that matter, facilitates the analysis of such data. One should be looking for conditions where all bands contribute significantly to the intensity spectrum. These are measured much faster than spin asymmetries and can therefore be used for a fast screening before acquiring spin-resolved data. For the photon energies of 25 and 33 eV, a Rashba-type spin splitting could be concluded without fitting the data, because the spin polarization curves show a typical down-up down-up scenario in the y-component [14]. Nevertheless, our examples show that the two-step fitting routine can also handle situations with rather weak contributions from some of the peaks, with correspondingly larger error bars in the spin polarization vector components. For instance, the two-step fitting routine would unravel that the weak signal corresponding to the band '$r2$' at 21.2 and 23 eV (figure 12) needs to have a spin polarization opposite to '$r1$' and thus confirm a Rashba-type scenario. In any case, the two-step fitting routine is required in order to quantify the spin polarization vectors.

7. Conclusions and outlook

It appears that spectacular developments in spintronics and in new topological phases on surfaces have created renewed and strong interest in spin-polarized photoemission experiments. While this paper has attempted to cover new methodical aspects of the analysis of such data in a tutorial way, a more systematic review on recent SARPES experiments on non-magnetic reduced-dimensional systems has very recently been published elsewhere by one of the authors [28]. The number of such instruments increases steadily, and recent progress in spin detection efficiencies, using spin polarimeters based on exchange scattering off oxidized iron films grown on W(001) [29] or on MgO(001) [30], promises data acquisition rates that are two orders of magnitude faster than with current instruments using conventional Mott detectors. More importantly, one will no longer need to sacrifice spectrometer resolution in favor of high transmission, opening up an entirely new world in high-resolution SARPES. In this context, the quantitative analysis tools presented in this paper will find wide application in order to

quantify spin polarization vectors of individual bands, or to separate bands with even tinier spin splittings, in an even wider range of materials, including strongly correlated electron systems. Spin polarization should be ubiquitous when measuring with high enough resolution!

Acknowledgments

We are indebted to Moritz Hoesch, Jorge Lobo-Checa, Vladimir Petrov, Matthias Muntwiler, Matthias Hengsberger, Taichi Okuda, Thomas Greber, Luc Patthey, Werner Deichmann and Martin Klöckner for their contributions in building the end station COPHEE at the Swiss Light Source, a unique facility for SARPES experiments at the Paul Scherrer Institut. Further, we thank J Henk and G Bihlmayer for valuable discussions about spin–orbit effects in metallic surface states. This work has been supported by the Swiss National Science Foundation.

References

[1] Datta S and Das B 1990 *Appl. Phys. Lett.* **56** 665
[2] Bychkov Y A and Rashba E I 1984 *JETP Lett.* **39** 78
[3] Ast C R, Henk J, Ernst A, Moreschini L, Falub M C, Pacilé D, Bruno P, Kern K and Grioni M 2007 *Phys. Rev. Lett.* **98** 186807
[4] Kane C L and Mele E J 2005 *Phys. Rev. Lett.* **95** 146802
[5] Hsieh D, Qian D, Wray L, Xia Y, Hor Y S, Cava R J and Hasan M Z 2008 *Nature* **452** 970
[6] Bernevig B A, Hughes T L and Zhang S-C 2006 *Science* **314** 1757
[7] Hüfner S 2003 *Photoelectron Spectroscopy: Principles and Applications* 3rd edn (Berlin: Springer)
[8] Hopster H, Raue R, Güntherodt G, Kisker E, Clauberg R and Campagna M 1983 *Phys. Rev. Lett.* **51** 829
[9] Kessler J 1985 *Polarized Electrons* 2nd edn (Berlin: Springer)
[10] Heinzmann U and Schönhense G 1985 Spin-resolved photoemission from nonmagnetic metals and adsorbates *Polarized Electrons in Surface Physics* ed R Feder (Singapore: World Scientific) pp 467–512
[11] Osterwalder J 2006 Spin-polarized photoemission *Magnetism: Synchrotron A Radiation Approach* (*Lecture Notes in Physics* vol 697) ed E Beaurepaire, H Bulou, F Scheurer and J-P Kappler (Berlin: Springer) pp 95–120
[12] Muntwiler M, Hoesch M, Petrov V N, Hengsberger M, Patthey L, Shi M, Falub M, Greber T and Osterwalder J 2004 *J. Electron Spectrosc. Relat. Phenom* **137–140** 119
[13] Meier F, Dil H, Lobo-Checa J, Patthey L and Osterwalder J 2008 *Phys. Rev.* B **77** 165431
[14] Hoesch M, Muntwiler M, Petrov V N, Hengsberger M, Patthey L, Shi M, Falub M, Greber T and Osterwalder J 2004 *Phys. Rev.* B **69** 241401
[15] Hsieh D *et al* 2009 *Science* **232** 919
[16] Dil J H, Meier F, Lobo-Checa J, Patthey L, Bihlmayer G and Osterwalder J 2008 *Phys. Rev. Lett.* **101** 266802
[17] Gay T J and Dunning F B 1992 *Rev. Sci. Instrum.* **63** 1635
[18] Gellrich A and Kessler J 1991 *Phys. Rev.* A **43** 204
[19] Hoesch M, Greber T, Petrov V N, Muntwiler M, Hengsberger M, Auwärter W and Osterwalder J 2002 *J. Electron Spectrosc. Relat. Phenom.* **124** 263
[20] Premper J, Trautmann M, Henk J and Bruno P 2007 *Phys. Rev.* B **76** 073310
[21] LaShell S, McDougall B A and Jensen E 1996 *Phys. Rev. Lett.* **77** 3419
[22] Pacilé D, Ast C R, Papagno M, Da Silva C, Moreschini L, Falub M, Seitsonen A P and Grioni M 2006 *Phys. Rev.* B **73** 245429
[23] Bihlmayer G, Bluegel S and Chulkov E V 2007 *Phys. Rev.* B **75** 195414
[24] Petrov V N, Galaktionov M S and Kamochkin A S 2001 *Rev. Sci. Instrum.* **72** 3729

[25] Armstrong B H 1967 *J. Quant. Spectrosc. Radiat. Transfer* **7** 61
[26] Henk J, Hoesch M, Osterwalder J, Ernst A and Bruno P 2004 *J. Phys.: Condens. Matter* **16** 7581
[27] Cacho C M, Vlaic S, Malvestuto M, Ressel B, Seddon E A and Parmigiani F 2009 *Rev. Sci. Instrum.* **80** 043904
[28] Dil J H 2009 *J. Phys.: Condens. Matter* **21** 403001
[29] Winkelmann A, Hartung D, Engelhard H, Chiang C-T and Kirschner J 2008 *Rev. Sci. Instrum.* **79** 083303
[30] Okuda T, Takeichi Y, Maeda Y, Harasawa A, Matsuda I, Kinoshita T and Kakizaki A 2008 *Rev. Sci. Instrum.* **79** 123117